Origin of high-T_c superconductivity in doped Hubbard models and their extensions: Roles of uniform charge fluctuations

Takahiro Misawa and Masatoshi Imada
Department of Applied Physics, University of Tokyo, 7-3-1 Hongo, Bunkyo-ku, Tokyo 113-8656, Japan
(Received 23 October 2013; revised manuscript received 2 September 2014; published 22 September 2014)

The doped Hubbard model is a simple model for high-T_c cuprate superconductors, while its ground state remains a challenge. Here, by performing state-of-the-art variational Monte Carlo calculations for the strong-coupling Hubbard model, we find evidence that the d-wave superconducting phase emerges always near the phase separation region and the superconducting order has one-to-one correspondence with the enhancement of charge compressibility. The order as well as the phase separation are vulnerable to realistic intersite Coulomb interaction, while the superexchange interaction enhances both. An appropriate combination of these two widens the stable superconducting phase.

DOI: 10.1103/PhysRevB.90.115137 PACS number(s): 71.10.Fd, 71.27.+a, 74.40.Kb, 74.72.−h

I. INTRODUCTION

The discovery of high-T_c superconductivity in copper oxides [1] triggers studies of the superconductivity induced by strong electronic correlations. After an enormous number of studies, the intrinsic phase diagram of the copper oxides is still not a completely resolved issue. Most of the superconducting copper oxides have the dome structure of the critical temperature T_c as a function of the hole doping concentration δ centered at the optimum value, $\sim$0.15, after the quick disappearance of the antiferromagnetic order upon doping to the Mott insulator of the mother materials.

However, the multilayer compound shows a wide coexistence region of superconductivity and antiferromagnetic order [2]. Recently the interface of $La_2CuO_4/La_{2-x}Sr_xCuO_4$, which is expected to realize purely two-dimensional superconductivity, has strikingly shown a pinning of T_c at a constant value of $\sim$40 K [3], in marked contrast with the dome structure in bulk, which supports that the intrinsic nature of the copper oxides is described by an extended region of the phase separation (PS), if the long-ranged Coulomb interaction is screened by the interlayer screening. At the interface, the phase separation may occur between layers. The intrinsic phase diagram of the copper oxides without impurity and long-ranged Coulomb effects are still an actively debated issue.

One of the most fundamental models to describe high-T_c superconductivity is the Hubbard model on the square lattice, which only considers the nearest-neighbor hopping t and on-site Coulomb repulsion U of electrons (details are shown in Sec. II). A large number of theoretical works, including analytical and numerical calculations, have been devoted to the Hubbard model [4–16]. (A detailed comparison of previous studies is given in Appendix A.) Many works suggest that the superconductivity appears near half band filling for sufficiently large U/t [6–15,17]. However, numerically exact or high-precision calculations [4,5,16] do not necessarily show clear evidence of high-T_c superconductivity. Thus, the relation between strong electronic correlations and high-T_c superconductivity still remains an unresolved issue, although there are many proposals as to the origin of the high-T_c superconductivity [4,8,10,13,14,17–27]. The Hubbard model tremendously simplifies the real materials. However, the prolonged controversy implies the significance of clarifying the superconductivity in the doped Hubbard models to understand the fundamental origin of the high-T_c superconductivity, provided that reliable theoretical calculations are performed.

In this paper, by performing state-of-the-art calculations, we show a direct and quantitative one-to-one correspondence between superconductivity and enhanced uniform charge susceptibility, which clearly shows that the tendency for the PS is the origin of the d-wave superconductivity. The present result also offers an intriguing implication to the recent interface experiment [3]. We further reveal roles of intersite Coulomb repulsion V that reduce both the superconducting phase and uniform charge fluctuations, as well as the roles of the superexchange interaction J that enhances both of them.

II. MODEL, METHOD, AND DEFINITIONS OF PHYSICAL QUANTITIES

We employ the standard Hubbard model on the square lattice, defined by the Hamiltonian

$$H = -t \sum_{\langle i,j\rangle,\sigma} (c^\dagger_{i\sigma} c_{j\sigma} + \text{H.c.}) + U \sum_i n_{i\uparrow} n_{i\downarrow},$$

where $c^\dagger_{i\sigma}$ ($c_{i\sigma}$) is the creation (annihilation) operator on the ith site with spin σ, and $n_{i\sigma} = c^\dagger_{i\sigma} c_{i\sigma}$ is the number operator. The transfer integral t is only taken for nearest-neighbor sites. We take $N_s = L \times L$ sites with periodic-periodic (PP) and antiperiodic-periodic (AP) boundary conditions. We define the doping rate δ as $\delta = 1 - N_e/N_s$, where $N_e = \sum_{i,\sigma} n_{i\sigma}$. We add the off-site Coulomb and superexchange interactions defined as

$$H_V = V \sum_{\langle i,j\rangle} n_i n_j,$$

$$H_J = J \sum_{\langle i,j\rangle} \boldsymbol{S}_i \cdot \boldsymbol{S}_j,$$

where $\boldsymbol{S}_i = 1/2 \sum_{\sigma,\sigma'} c^\dagger_{i,\sigma} \boldsymbol{\sigma}_{\sigma,\sigma'} c_{i,\sigma'}$ and $n_i = n_{i\uparrow} + n_{i\downarrow}$.

To study the ground state of the doped Hubbard model, we employ a many-variable variational Monte Carlo (mVMC) method combined with the quantum-number projection. Our

variational wave function is defined as

$$|\psi\rangle = \mathcal{P}_{\rm G}\mathcal{P}_{\rm J}\mathcal{P}^{\rm ex}_{\rm d-h}\mathcal{L}^{K=0}\mathcal{L}^{S=0}|\phi_{\rm pair}\rangle, \quad (1)$$

where $\mathcal{P}_{\rm G}$, $\mathcal{P}_{\rm J}$, $\mathcal{P}^{\rm ex}_{\rm d-h}$ are the Gutzwiller [28], Jastrow [29,30], and doublon-holon correlation factors [31], respectively [32]. The Gutzwiller factor punishes the double occupation of electrons on the same site through the variational parameters g, defined as

$$\mathcal{P}_{\rm G} = \exp\left(-g\sum_i n_{i\uparrow}n_{i\downarrow}\right).$$

The Jastrow factors are defined as

$$\mathcal{P}_{\rm J} = \exp\left(-\frac{1}{2}\sum_{i,j} v_{ij}n_i n_j\right),$$

where the long-range part drives the distinction between the metal and insulator [30]. The doublon-holon correlation factors [31] are defined as

$$\mathcal{P}^{\rm ex}_{\rm d-h} = \exp\left[-\sum_{m=0}^{2}\sum_{\ell=1,2}\alpha^{(\ell)}_{(m)}\sum_i \xi^{(\ell)}_{i(m)}\right],$$

where $\xi^{(\ell)}_{i(m)}$ is a many-body operator which is diagonal in the real-space representations. When a doublon (holon) exists at the ith site and m holons (doublons) surround at the ℓth nearest neighbor, $\xi^{(\ell)}_{i(m)}$ gives 1. Otherwise, $\xi^{(\ell)}_{i(m)}$ gives 0. The spin (momentum) quantum number projection operator $\mathcal{L}^{S=0}$ ($\mathcal{L}^{K=0}$) restores SU(2) spin symmetry (translational symmetry) with the total spin $S=0$ (total momentum $K=0$). These projections substantially improve the accuracy of cluster properties, make the size dependence smaller, and the extrapolation to the thermodynamic limit easier [32].

The one-body part $|\phi_{\rm pair}\rangle$ is the generalized pairing wave function defined as

$$|\phi_{\rm pair}\rangle = \left[\sum_{i,j=1}^{N_{\rm s}} f_{ij}c^\dagger_{i\uparrow}c^\dagger_{j\downarrow}\right]^{N_e/2}|0\rangle, \quad (2)$$

where f_{ij} denotes the variational parameters. (For details of f_{ij}, see Refs. [32–34]). In this study, we allow f_{ij} to have a 2×2 sublattice structure or equivalently, we have $2\times 2\times N_{\rm s}$ independent variational parameters for the one-body part. All the variational parameters are simultaneously optimized by using the stochastic reconfiguration method [32,35]. The variational function $|\psi\rangle$ in Eq. (1) can flexibly describe paramagnetic metals, the antiferromagnetic phase, and superconducting phases as well as their fluctuations and/or coexistence. It is important to fully optimize the long-range part of f_{ij} to realize states with strong fluctuations and well-developed, short-ranged order as well as strongly renormalized metals, as we detail later. Actually, by extending the 2×2 sublattice structures of the variational parameters f_{ij}, we confirmed that the accuracy of the energy is improved.

Furthermore, by applying the power Lanczos method [36], we can also substantially improve the energy. In the Nth-step power Lanczos method, we multiply the Hamiltonian to the variational wave functions as follows:

$$|\psi_n\rangle = \left(1+\sum_{n=1}^{N}\alpha_n H^n\right)|\psi\rangle, \quad (3)$$

where α_n are the variational parameters. By choosing α_n to lower the energy, we can systematically improve the variational wave functions, as we see later in Fig. 7. However, through the careful examination of such extensions, we confirmed that estimates of the physical properties (superconducting correlations, antiferromagnetic correlations, etc.) change little (for example, see Fig. 1). In addition, the numerical cost of such extensions is demanding. Therefore, to perform the comprehensive calculations for the doped Hubbard with additional intersite interactions, we have used the present tractable variational wave functions. Nevertheless, we again emphasize that the estimates of the physical properties themselves are accurate enough and our conclusions do not change.

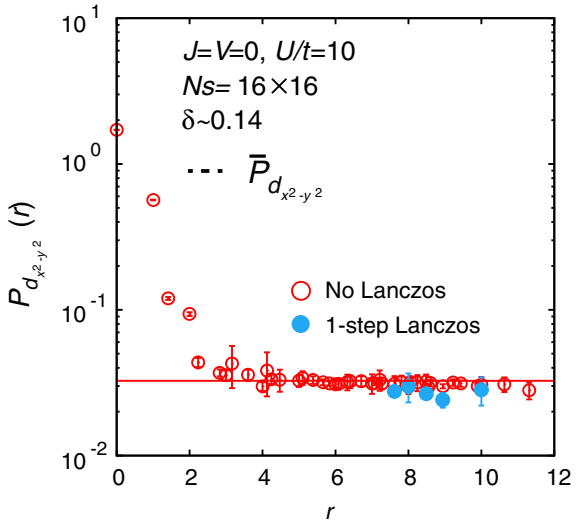

FIG. 1. (Color online) Distance (r) dependence of superconducting correlation for $\delta\sim 0.14$, $J=V=0$, and $U/t=10$. The system size is $N_{\rm s}=16\times 16$, and the AP boundary condition is used. Results of first-step Lanczos method are shown by (light blue) closed circles.

To discuss the condensation energy, we generate two different wave functions, i.e., normal and superconducting wave functions, by choosing proper initial states. We employ the noninteracting Fermi sea for the normal state, and the BCS d-wave superconductivity state for the superconducting phase as the initial states [32]. By optimizing these initial states, we obtain normal and superconducting states. In the strong-coupling region, the antiferromagnetic order appears near half filling as the normal state as a result of the optimization, although we do not assume the antiferromagnetic order as an initial state, which means that the paramagnetic normal state is unstable.

To determine the ground state of the doped Hubbard model, we calculate the spin structure factor and the equal-time superconducting correlation. The spin structure factor is

defined as

$$S(\boldsymbol{q}) = \frac{1}{3N_s}\sum_{i,j}\langle \boldsymbol{S}_i \cdot \boldsymbol{S}_j\rangle e^{i\boldsymbol{q}\cdot(\boldsymbol{r}_i-\boldsymbol{r}_j)},$$

and the equal-time superconducting correlations are defined as

$$P_\alpha(\boldsymbol{r}) = \frac{1}{2N_s}\sum_{\boldsymbol{r}_i}\langle \Delta_\alpha^\dagger(\boldsymbol{r}_i)\Delta_\alpha(\boldsymbol{r}_i+\boldsymbol{r}) + \Delta_\alpha(\boldsymbol{r}_i)\Delta_\alpha^\dagger(\boldsymbol{r}_i+\boldsymbol{r})\rangle.$$

In actual calculations, to reduce numerical cost, we restrict the summation with respect $\boldsymbol{r}_i$ to $\boldsymbol{r}_i = 0$. Superconducting order parameters $\Delta_\alpha(\boldsymbol{r}_i)$ are defined as

$$\Delta_\alpha(\boldsymbol{r}_i) = \frac{1}{\sqrt{2}}\sum_{\boldsymbol{r}} f_\alpha(\boldsymbol{r})\left(c_{\boldsymbol{r}_i\uparrow}c_{\boldsymbol{r}_i+\boldsymbol{r}\downarrow} - c_{\boldsymbol{r}_i\downarrow}c_{\boldsymbol{r}_i+\boldsymbol{r}\uparrow}\right).$$

Here $f_\alpha(\boldsymbol{r})$ is the form factor that describes the symmetry of the superconductivity. For $d_{x^2-y^2}$ superconductivity, we define

$$f_{d_{x^2-y^2}}(\boldsymbol{r}) = \delta_{r_y,0}\left(\delta_{r_x,1}+\delta_{r_x,-1}\right) - \delta_{r_x,0}\left(\delta_{r_y,1}+\delta_{r_y,-1}\right),$$

where $\delta_{i,j}$ denotes the Kronecker delta and $\boldsymbol{r} = (r_x, r_y)$. We define the long-range average of the superconducting correlation as

$$\bar{P}_{d_{x^2-y^2}} = \frac{1}{M}\sum_{2<r=|\boldsymbol{r}|<L-1} P_{d_{x^2-y^2}}(\boldsymbol{r}),$$

where M is the number of vectors satisfying $2 < r < L-1$. As shown in Fig. 1, the criterion $r > 2$ is, within the present purpose, practically a sufficient probe to see whether the pairing order-parameter correlation is saturated to a nonzero value and offers a good measure for the square of the order parameter in the long-range ordered superconducting state. We also note that the first-step power Lanczos method does not essentially change the superconducting correlations, as we see in Fig. 1.

We also calculate the chemical potential by using the relation

$$\mu(\bar{N}) = \{E(N_1) - E(N_2)\}/\{N_1 - N_2\} - \frac{U}{2}, \qquad (4)$$

where $E(N_1)$ is the total energy at filling N_1 and $\bar{N} = (N_1 + N_2)/2$. To directly compare with previous calculations [4,37], we subtract the constant value $U/2$. To reduce the finite-size effects, we perform calculation only at the electron densities that satisfy the closed-shell condition in the noninteracting case [4,37].

The nonzero condensation energy $\Delta E = (E_{\rm SC} - E_{\rm Normal})/N_s$ is defined when the superconducting (with energy $E_{\rm SC}$) and normal states ($E_{\rm Normal}$) exist as local minima. The normal state is not necessarily the paramagnetic state but can be another symmetry-broken state such as the antiferromagnetically ordered state, if it has a lower energy than the paramagnetic state. It is remarkable that in the present calculation, if the superconducting state with a nonzero order parameter exists, it always has a normal state as local minima as well. The transition from the normal to the superconducting states by reducing the doping concentration from the overdoped region is always a weak first-order transition where the superconducting order parameter jumps from zero to a small nonzero value in the ground state. For instance, as we show later, at $(V/t = 0, J/t = 0)$, $(V/t = 0, J/t = 0.5)$, $(V/t = 1, J/t = 0.5)$, and $(V/t = 2, J/t = 0.5)$, the superconducting state emerges as a metastable state at $\delta \sim 0.25, 0.33, 0.29, 0.28$ while it becomes the ground state only for $\delta \lesssim 0.22, 0.31, 0.27, 0.28$, respectively. The first-order jump decreases with the increase in V/t, suggesting an existence of the tricritical point at around $(V/t = 2,\ J/t = 0.5)$. Toward half filling, the order parameter of the superconducting state becomes continuously zero, before the emergence of the antiferromagnetic Mott insulator. Here, again, the nonsuperconducting state continues to exist as a metastable excited state.

In connection with the experimental measurement of the condensation energy by the specific heat or the upper critical field, the present definition is not exactly identical with each other because the normal state in the experiment usually excludes the magnetic order as the normal state, for instance. This means that the experimental value overestimates the true condensation energy. However, the present definition certainly gives a more useful criterion to determine whether the superconducting state is the true ground state or not.

The normal state is defined as the state that has vanishing superconducting order within the numerical accuracy. It does not exclude the possibility of a state with a tiny order parameter expected from the Kohn-Luttinger mechanism [38]. In addition, the normal state we obtained has a robust and developed superconducting correlation with the extended s-wave order parameter with the form factor $\cos k_x + \cos k_y$, which scales to zero in the thermodynamic limit within numerical accuracy.

A Monte Carlo sampling of real space configurations of the electrons is employed to calculate physical quantities following the standard procedure [32]. The number of Monte Carlo samples for the calculation of physical quantities is typically 128 000. The statistical error of the Monte Carlo sampling estimated from a number of independent computations is indicated in the last parentheses in the numerical data, as well as error bars in the plots in figures.

III. RESULTS

A. Simple Hubbard model ($V = J = 0$)

To examine the origin of high-T_c superconductivity in the Hubbard model, we employ the mVMC method [32]. (For the validity of the method, see Appendix B.) This method enables us to perform high-precision calculations under spatial and temporal fluctuations of spin and charge on equal footings with a sufficient flexibility of wave functions, which are important in strongly correlated systems.

Figure 2 shows the doping dependence of several physical properties for $U/t = 10$: the peak value of the spin structure factor $S(\boldsymbol{q}_{\rm peak})/N_s$, which is the square of the antiferromagnetic ordered moment, and average value of superconducting correlation $\bar{P}_{d_{x^2-y^2}}$ at long distance with the $d_{x^2-y^2}$ symmetry, corresponding to the square of the superconducting order parameter. We also plot the condensation energy ΔE.

We find the $d_{x^2-y^2}$-wave superconducting phase only in the strong-coupling region $U/t \gtrsim 6$, which is consistent with previous studies [4–6,8,10,11,15]. For instance, at $U/t = 10$, the d-wave superconductivity emerges for $\delta \lesssim 0.2$, as shown in Fig. 3. Both ΔE and $\bar{P}_{d_{x^2-y^2}}$ have dome structures around $\delta \sim$

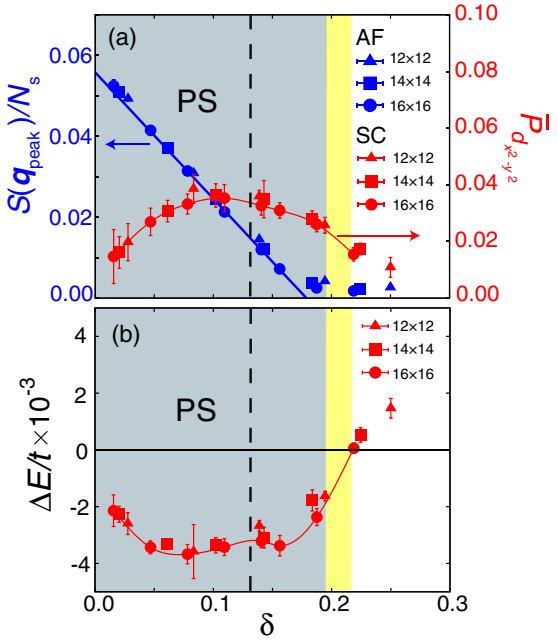

FIG. 2. (Color online) (a) Doping (δ) dependence of averaged $d_{x^2-y^2}$-wave superconducting correlations $\bar{P}_{x^2-y^2}$ and peak values of spin structure factors $S(\boldsymbol{q}_{\rm peak})$ for $U/t = 10$ and $V = J = 0$. Doping rate δ is defined as $\delta = 1 - N_e/N_s$, where N_e (N_s) represents the number of electrons (system size). We note that the incommensurate spin orders or stripe phases are not found in the relevant doping region $\delta \lesssim 0.2$, even when we employ large sublattice structures. We also note that the charge structure factors have no significant peak at $q \neq 0$. (b) Doping dependence of condensation energy ΔE. The condensation energy is defined as $\Delta E = (E_{\rm SC} - E_{\rm Normal})/N_s$, where $E_{\rm SC}$ ($E_{\rm Normal}$) is the total energy of the superconducting phase (normal phase). The calculations are performed for sizes of $N_s = 12\times12, 14\times14, 16\times16$ on the square lattice, and we confirm that the finite-size effects are negligibly small. The shaded region denotes the PS region and the black dashed line represents the spinodal point. Details of PS are shown in the main text and Fig. 3. The superconducting phase without PS remains only in the yellow region. In the present plots and the plots in the later figures, the error bars indicate the estimated statistical errors of the Monte Carlo sampling.

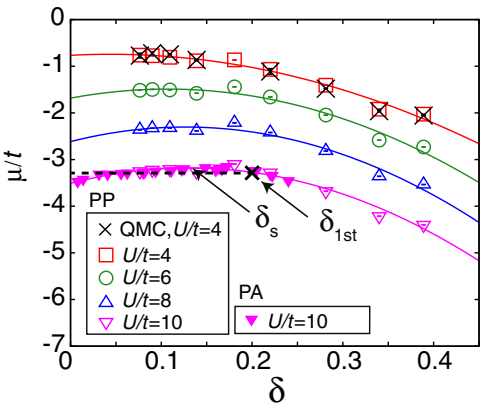

FIG. 3. (Color online) Doping dependence of chemical potential for $U/t = 4,8,6,10$, $V = J = 0$, and system sizes $L = 6,8,10,12,14,16$, where $N_s = L \times L$. We note that different size results are essentially on the same curve. For $U/t = 4$, our mVMC successfully reproduces the results of quantum Monte Carlo (QMC) represented by black crosses [4]. By fitting the chemical potential with the second-order polynomials, we estimate the spinodal point, where $(dn/d\mu)^{-1} = 0$. We also estimate the PS region ($\delta < \delta_{1st}$) by performing Maxwell's construction using the fitted second-order polynomials. Maxwell's construction for $U/t = 10$ is shown by the (black) dotted line. For $U/t = 10$, we estimate that the PS occurs for $\delta < \delta_{1st} \sim 0.195$. We also estimate that the spinodal point, in which the charge compressibility diverges ($\chi_c^{-1} = 0$), is located at $\delta_s \sim 0.178$ for $U/t = 10$. To ensure the existence of the PS, we further perform the first-step power Lanczos calculations (see Fig. 19 in Appendix F) and confirm that the Lanczos step changes μ little. This result indicates that little improvement of energy affects the PS region.

0.1. The antiferromagnetic quantum critical point (AFQCP) where the antiferromagnetic spin fluctuations diverge appears at $\delta \sim 0.18$. The d-wave superconductivity coexists with the antiferromagnetism in the ground state for $\delta \lesssim 0.18$. The coexistence has been theoretically studied before in several different contexts [8,10,39,40]. The coexistence is basically consistent with the multilayer cuprates [2], where the PS may be suppressed by the interlayer self-doping.

To examine the effects of charge fluctuations, the doping dependence of the chemical potential μ is shown in Fig. 3, where the uniform charge susceptibility $\chi_c \equiv dn/d\mu$ monitors the charge fluctuation. (See Appendix E for the charge structure factor in the PS region.) The spinodal point of doping (δ_s), where charge fluctuations diverge ($\chi_c^{-1} = 0$), is found to increase at larger U. Accordingly, the PS region becomes wider by increasing U/t. If we enforce the charge uniformity, the superconducting correlation has a maximum at around $\delta_s \sim 0.14$ (the spinodal point depicted by the dashed black line in Fig. 2) for $U/t = 10$. This indicates that the enhanced charge fluctuations stabilize the superconducting phase at around half filling.

However, if the long-range Coulomb interaction is suppressed as in the Hubbard model, the present result indicates that in a wide region of the nominal doping concentration, the system undergoes a real-space PS into the antiferromagnetic Mott insulator and the superconducting region with the pinned T_c. This prediction is in striking agreement with the recent interfacial superconductivity [3].

B. Effects of intersite interactions

Here, to control the charge fluctuations, we introduce nearest-neighbor Coulomb interactions V ($H_V = V \sum_{\langle i,j\rangle} n_i n_j$), which inevitably exit in real materials. (See also Appendix A for previous studies.) As we see in Fig. 4, although a small $V/t = 1$ drastically shrinks the PS region (gray shaded region), the antiferromagnetic ordered moment and the AFQCP do not change appreciably. Although the superconducting correlations show a peak around the AFQCP, the condensation energy is largely reduced to almost zero, as shown in the inset of Fig. 4. This result supports the fact that the superconducting phase is predominantly stabilized by the enhanced charge fluctuations. We note that the next-nearest hopping t' destabilizes the superconductivity

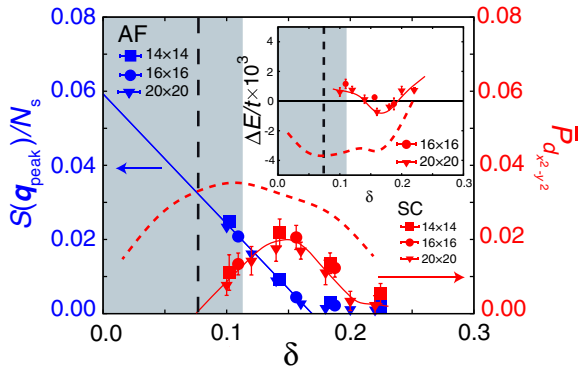

FIG. 4. (Color online) (a) Doping dependence of $\bar{P}_{x^2-y^2}$ and $S(\boldsymbol{q}_{\rm peak})$ at $V/t = 1$, $U/t = 10$, and $J = 0$ for the superconducting phase. In the inset, condensation energy ΔE is plotted as a function of δ. For comparison, we plot results of $U/t = 10$ and $V/t = 0$ by broken lines. The calculation has been done up to 20×20 lattices. Notations are the same as Fig. 2.

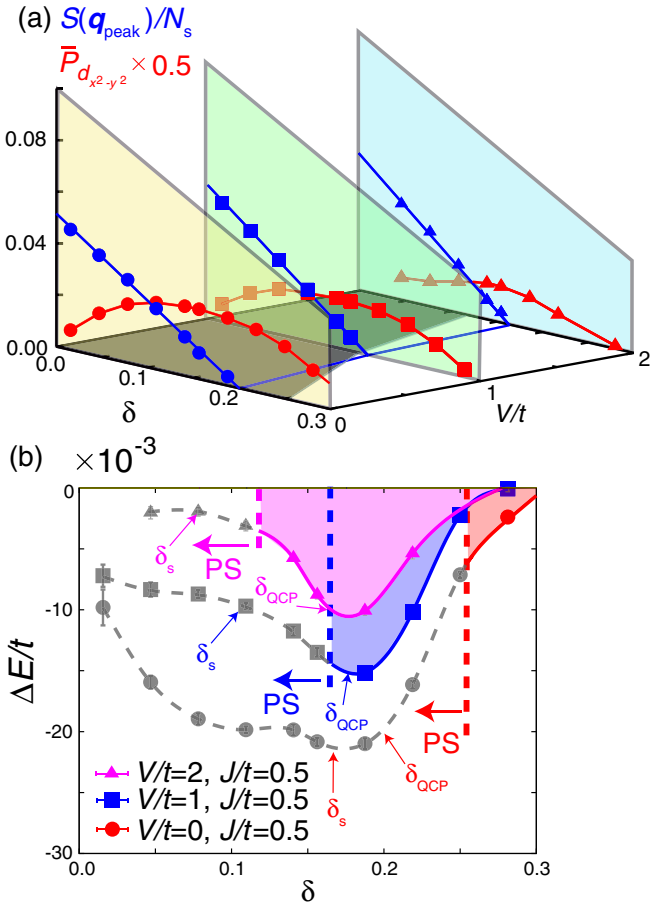

FIG. 5. (Color online) (a) Doping dependence of $\bar{P}_{x^2-y^2}$ and $S(\boldsymbol{q}_{\rm peak})$ for $V/t = 0,1,2$ and fixed $U/t = 10$ and $J/t = 0.5$. Additional J significantly enhances the superconducting correlations (see also Fig. 13). The shaded region and the blue line in the bottom panel represent the PS region and the position of the AFQCP, respectively. (b) Condensation energy as a function of δ. In the PS region, condensation energy is plotted by gray symbols. The positions of the spinodal point (δ_s) and the AFQCP ($\delta_{\rm QCP}$) are also plotted. Solid and broken curves are guides for the eyes.

in accordance with the shrinkage of the PS, which corroborates this conclusion (see also Appendix D).

It is also an intriguing issue to examine whether the instability toward the phase separation at the wave number $q = 0$ can be converted into the instability toward charge ordering at nonzero q, observed in some cases of the cuprates by employing realistic off-site Coulomb interactions. In this calculation, we do not find any signatures of the charge ordering, as shown in Fig. 18 in Appendix E.

To further understand the interplay of spin fluctuations and the instability toward the PS, by keeping $V = 0$, we introduce the nearest-neighbor superexchange interactions J ($H_J = J\sum_{\langle i,j\rangle} \boldsymbol{S}_i \cdot \boldsymbol{S}_j$) that do not follow the standard relation $J_{\rm eff} \sim 4t^2/U$. In reality, J can be induced by the d-p hybridizations in cuprate superconductors beyond the single-band framework [41–43]. It has been repeatedly discussed in the literature that the superexchange interaction is derived from the three-band d-p model for the cuprate superconductors in a nontrivial fashion without resorting to the single-band Hubbard model. Indeed, the Zhang-Rice singlet [41] produces the superexchange term J, which is rather independent of the expectation from the single-band Hubbard model in the strong-coupling limit. There exist several attempts to understand spin-dependent residual interactions within the single-band description but beyond the Hubbard model, with a finite U but with an additional J [42,43], while it is not well settled how the residual spin-dependent interaction should emerge quantitatively within the single-band approach. In this circumstance, it is helpful and insightful to understand the role of residual superexchange-type interaction in the mechanism of superconductivity by taking the amplitude of J as a parameter.

As illustrated in Fig. 5(a), finite $J/t = 0.5$ largely enhances the PS region, while the antiferromagnetic order does not change appreciably. Accompanied by the enhanced charge fluctuations, the condensation energy becomes an order of magnitude larger. Because the AFQCP is close to the spinodal point, as shown in Fig. 5(b), this significantly enhanced superconducting phase may be understood from the synergetic effects of spin and charge fluctuations. We later emphasize the importance of *short-ranged* fluctuations; however, this phase is again preempted by the PS.

In addition to J/t, we again add V. As we see in Fig. 5(a), by increasing V/t, locations of AFQCP do not change appreciably, while locations of the spinodal point rapidly approach half filling. In connection with the suppressed charge fluctuations, the condensation energy is significantly reduced, again suggesting the key role of the proximity of the PS in establishing high-T_c superconductivity. However, it is remarkable that, for the coexisting J and V, the superconducting phase with a substantial condensation energy survives in a wide range ($0.1 \lesssim \delta \lesssim 0.3$ for $V/t = 2$) outside the PS region.

The large condensation energy is ascribed mainly to two local sources: One is that the double occupancy D is largely reduced in the superconducting phase than that in the normal phase, which leads to the gain in the on-site Coulomb energy. This is because, the d-wave pair prohibits the

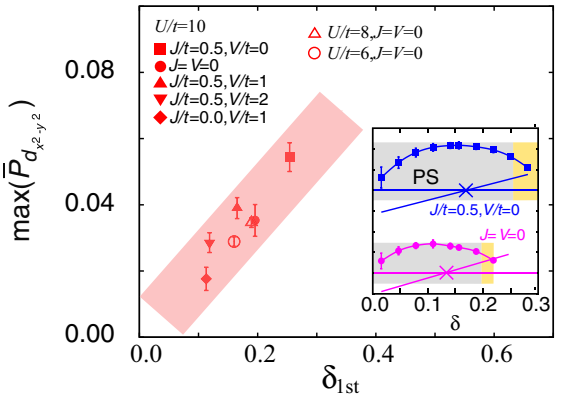

FIG. 6. (Color online) Relation between the peak value of the superconducting correlation $\max(\bar{P}_{d_{x^2-y^2}})$ and the strength of enhancement of charge fluctuations characterized by width of the PS region δ_{1st}. Inset: Doping concentration dependence of $20\times\bar{P}_{d_{x^2-y^2}}$ (curves with symbols) and $0.1\times\chi_c^{-1}$ (lines passing crosses) for two examples with offset in the ordinate for clarity. The crosses represent the spinodal point $\chi_c \to \infty$. The notation for the shaded zone is the same as Fig. 2.

double occupation strictly by symmetry, which is particularly effective when D remains larger in the normal phase (as around $\delta \sim 0.1$). (Figure 12 shows how the reduced D in the superconducting state enhances ΔE.) This mechanism cannot be captured by the t-J model. If $J > 0$, the other source is the antiferromagnetic correlation $\boldsymbol{S}_i \cdot \boldsymbol{S}_j$. The superconducting order enhances the underlying nearest-neighbor "antiferromagnetic" correlations even when $J = 0$, which provides the energy gain immediately when $J > 0$ (see Appendix C). The long-range part of antiferromagnetic correlation does not directly contribute to this gain.

The strong-coupling nature of high-T_c superconductivity emerges *not* from the long-ranged part and the quantum criticality, but rather from the local binding, as expected when approaching the regime of BEC. This local attractive interaction leads to Cooper pairing but does not necessarily lead to PS. This is because the PS signaled by the convex curve with a peak structure in the chemical potential as in Fig. 3 is mainly caused by the contribution of the kinetic-energy part in the chemical potential, which is evidenced in Fig. 14 of Appendix C. This peak in the kinetic energy is efficiently suppressed by V rather independently of the emergence of the local attractive interaction. While V suppresses PS, some choices of V and J largely strengthen the energy gain from D because of the enhanced D in the normal state. This is the reason why an appropriate combination of V and J stabilizes the high-T_c superconductivity without PS in an extended region. This implies that the superconducting stability is not a universal property but largely relies on material details. It requires a reexamination of the conditions for the emergence of high-T_c superconductivity. The necessity of both V and J also requires careful analyses regarding how they are derived quantitatively from first principles.

To see the relation between enhanced uniform charge fluctuations and the stability of superconductivity, we plot in Fig. 6 the relation between the maximum value of $\bar{P}_{d_{x^2-y^2}}$ and the width of the PS region in various cases of the superconducting state (main panel). A wider PS region indicates that charge fluctuation becomes more enhanced. The relation shows a clear correlation between $\max(\bar{P}_{d_{x^2-y^2}})$ and the PS region, indicating that the enhanced charge fluctuation stabilizes the superconductivity [26]. In the inset we plot the doping concentration dependence of the superconducting correlation and χ_c^{-1} for two typical examples. In addition to the correspondence between $\max(\bar{P}_{d_{x^2-y^2}})$ and the PS region, in all the cases we studied, the peaks of $\bar{P}_{d_{x^2-y^2}}$ are located at concentrations close to the spinodal points (crosses), indicating again the one-to-one correspondence between $\bar{P}_{d_{x^2-y^2}}$ and the charge fluctuation.

IV. SUMMARY

To summarize, the origin of the high-T_c superconducting phase in the doped Hubbard model is found primarily as arising from the phase separation instability. This conclusion suggests that the high-T_c superconductivity is not necessarily a generic property of the doped Mott insulators but depends sensitively on the material specific parameters, particularly on the intersite interactions, which gives a clue to understand the strong material dependence of T_c. Realistic intersite Coulomb repulsions V alone, which are often ignored in the literature, are severely destructive to superconductivity. However, they significantly contribute to widening the high-T_c superconducting region without phase separation, if properly combined with the antiferromagnetic correlations such as superexchange J.

Controlling the charge fluctuation through the off-site interactions, possibly by tuning a screening layer adjacent to the conducting layer, and control of the dielectric constant offers a possible way to stabilize the high-T_c superconducting phase. Though it is not so easy, an interesting future issue is to find a way to suppress the ratio of the off-site to on-site interactions by keeping a large on-site interaction in real materials with the help of *ab initio* calculations [44]. In this respect, the recently studied interfacial superconductivity [3] offers a promising solution and supports the relevance of the present phase diagram, with an extended region of PS as a genuine property of CuO_2 plane, if the long-ranged Coulomb interaction is screened on a single layer by capacitor formation with the neighboring metallic layers.

ACKNOWLEDGMENTS

The authors thank Daisuke Tahara and Satoshi Morita for providing them with efficient mVMC codes. To compute the Pfaffian of skew-symmetric matrices, we employ the PFAPACK [45]. A part of the algorithms used in exact diagonalization is based on TITPACK version 2, coded by Hidetoshi Nishimori. They also thank Antoine Georges for helpful comments. This work is financially supported by the MEXT HPCI Strategic Programs for Innovative Research (SPIRE) and the Computational Materials Science Initiative (CMSI). Numerical calculation was partly carried out at the Supercomputer Center, Institute for Solid State Physics, University of Tokyo. Numerical calculation was also partly carried out at K computer at the RIKEN Advanced Institute for

Computational Science (AICS) under Grants No. hp120043, No. hp120283, and No. hp130007. This work was also supported by a Grant-in-Aid for Scientific Research (No. 22104010, No. 22340090, and No. 23740261) from Ministry of Education, Culture, Sports, Science and Technology, Japan.

APPENDIX A: COMPARISON WITH PREVIOUS STUDIES

In Table I, we summarize the previous numerical studies on the doped Hubbard model. We summarize estimates of T_c, the region of the superconducting (SC) phase, and the antiferromagnetic (AF) phase. We also summarize information on phase separation (PS) and condensation energy ΔE. In the first column, the results of the present study are summarized. In the second column, we show several Monte Carlo, i.e., auxiliary-field quantum Monte Carlo (QMC) and Gaussian-basis quantum Monte Carlo (GBMC), as well as path-integral renormalization group (PIRG) calculations. We note that these methods do not restrict the form of the wave function *a priori* and give accurate estimates of the energy among various numerical schemes, if the interaction is from a weak to intermediate coupling region ($U/t \lesssim 6$). The accuracy of the PIRG has been benchmarked to be accurate [50] and applied to various cases [50–52]. The GBMC has been benchmarked

TABLE I. List of previous studies on the doped Hubbard model. SC, AF (AFM/AFI), PS, TABC, and GS represent superconductivity, antiferromagnetic (antiferromagnetic metal/insulator), phase separation, twist-averaged boundary condition, and ground state, respectively.

Authors [Method]	T_c	U/t	SC	AF	PS	ΔE
Present study [mVMC]	–(GS)	4–12	$\delta \lesssim 0.2$[a]	$\delta \lesssim 0.18$	$\delta \lesssim 0.19$[b]	$\sim 0.004t$
Furukawa and Imada (1992) [4] [QMC]	–(GS)	4	No SC	No AF	No PS	
Watanabe and Imada (2004) [46] [PIRG][c]	–(GS)	4	No SC	No AF	No PS	
Aimi and Imada (2007) [5] [GBMC]	–(GS)	4–6	No SC	No AF		
Maier *et al.* (2004) [7] [DCA]	$\sim 0.02t$	4	$\delta \sim 0.1$			
Khatami *et al.* (2010) [9] [DCA]	$\sim 0.02t$	8	$\delta \lesssim 0.2$		QCP at $\delta \sim 0.9$	
Capone and Kotliar (2006) [10] [CDMFT]	–(GS)	4–16	$\delta \lesssim 0.15$[d]	$\delta \lesssim 0.15$	$0.05 \lesssim \delta \lesssim 0.15$[e]	$\sim 0.01t$[f]
Aichhorn *et al.* (2007) [8] [VCA] [g]	–(GS)	4–12	$\delta \lesssim 0.2$[h]	$\delta \lesssim 0.15$	$0.05 \lesssim \delta \lesssim 0.15$[i]	
Gull and Millis (2012) [12] [DCA]	$\sim 0.016t$	4–6.5	$\delta \lesssim 0.15$[j]			$\sim 0.01t$
Sordi *et al.* (2012) [11] [CDMFT]	$\sim 0.02t$	5.2–6.2	$\delta \lesssim 0.08$[k]		$0.04 \lesssim \delta \lesssim 0.06$[l]	
Giamarchi and Lhuillier (1991) [40] [VMC]	–(GS)	10	$\delta \lesssim 0.4$	$\delta \lesssim 0.2$[m]		
Yokoyama *et al.* (2004,2012) [6,47] [VMC]	–(GS)	0–30	$\delta \lesssim 0.2$[n]	$\delta \lesssim 0.15$	$\delta \lesssim 0.1$	$\sim 0.01t$
Eichenberger and Baeriswyl (2009) [15] [VMC]	–(GS)	6	$\delta \lesssim 0.2$	$\delta \lesssim 0.1$?		$\sim 0.01t$
Neuscamman *et al.* (2012) [23] [VMC][o]	–(GS)	4			$\delta \lesssim 0.15$[p]	
Zhang *et al.* (1997) [16] [CPMC][q]	–(GS)	2–8	No SC			
Chang *et al.* (2008, 2010) [21,48] [CPMC][r]	–(GS)	2–12		$\delta \lesssim 0.1$[s]	$\delta \lesssim 0.1$[t]	
Sorella (2011) [22] [VMC][u]	–(GS)	4			No PS	
Becca *et al.* (2000) [49] [GFMC]	–(GS)	4–10			No PS	
Tocchio *et al.* (2013) [25] [VMC]	–(GS)	6			No PS	-

[a] Only for $U/t \gtrsim 8$. It is absent for $U/t \lesssim 6$.
[b] $U/t = 10$ (SC-AFI).
[c] $t'/t = 0$ and -0.2.
[d] $U/t = 4$–16.
[e] $U/t = 16$ (AF-SC).
[f] SC-AFM, $U/t = 16$.
[g] $t'/t = -0.3$, where t' is the next-nearest-neighbor transfer.
[h] $U/t = 4$–12.
[i] $U/t = 8$ (SC-SC+AF).
[j] $U/t = 4$–6.5.
[k] $U/t = 5.2$–6.2.
[l] (Metal-metal).
[m] SC+AF.
[n] $U/t = 5$–30.
[o] $N_s = 8 \times 8$, TABC.
[p] (Metal-AFI?).
[q] $N_s \leqslant 16 \times 16$, PP.
[r] $N_s = 8 \times 8$–16×16, TABC.
[s] Incommensurate spin structures.
[t] For $U/t \geqslant 8$, a spatially inhomogeneous state is obtained.
[u] $N_s = 98$.

with the preprojection method [5], which substantially relaxes the limitation and eliminates the origin of the errors (boundary terms) [53] and then gives good agreement with the QMC results. The (high-T_c) superconducting phase does not appear in the region of $U/t \lesssim 6$ in all of these methods. The absence is consistent with the present mVMC result, i.e., we confirm that the superconducting phase is not stabilized for $U/t \lesssim 6$, as shown in the first column. This is consistent with some other results [15,47] as well as the constrained-path Monte Carlo (CPMC) studies[16].

At $U/t = 4$, the divergence of the compressibility is suggested at $\delta \sim 0$ [4,22], which means that the phase separation is absent but the system is close to the marginal quantum critical point [26,54]. The absence of the phase separation or restriction at most to a tiny region $\delta < 0.06$ [4,22,37,46,55] is well consistent with the present study. The phase separation is clearly observed in a wide region of the doping concentration in the present study for the strong-coupling region ($U/t > 6$), which has not been well studied before by quantitatively accurate methods.

In the third column, we mainly show the results obtained by dynamical mean-field theory (DMFT) calculations with cluster extension, such as the dynamical cluster approximation (DCA) and cellular DMFT (CDMFT). We also show the results of variational cluster approximations (VCA).

All of these works suggest that the d-wave superconducting phase appears at around $\delta \sim 0.1$. The absence of the superconductivity for $U \leqslant 6$ observed in the present study is not consistent with DMFT and its extensions [7,8,10–12], which may be attributed to the overestimation of the superconductivity in DMFT because of the mean-field approximation. We note that the presence or absence of the superconductivity is determined only by the long-ranged part of the pairing correlation, while such spatial correlations and fluctuations are not captured by the DMFT.

Some works suggest that the first-order phase transition between two metal phases occurs, i.e., phase separation occurs between metals [9]. This type of phase separation is only found in DMFT calculations and is not observed in other calculations such as VMC and CPMC, as shown in the fourth and fifth columns.

In the fourth column, we show several previous VMC calculations. In the previous VMC calculations, the form of wave functions is limited and they use different wave functions to describe the Fermi liquid, antiferromagnetic phase, d-wave superconducting phase, and their coexistence phase [40], respectively.

We typically obtain a 5% lower energy compared to early VMC results [47]. For example, for $U/t = 10$, $L = 10$, $\delta = 0.88$, and AP boundary conditions, Yokoyama *et al*. [47] obtain $E/N_s \sim -0.60t$ while we obtain $E/N_s \sim -0.625t$. Recent VMC studies implemented a number of additional improvements to reach better accuracy [22,25], which are comparable to the present study in energy. In contrast to most of the earlier studies, we employ a flexible one-body part of the wave functions defined in Eq. (2). By optimizing the long-range part of f_{ij}, this wave function can describe insulators to antiferromagnetic metals, superconducting phases, strongly correlated metals and their competitions or coexistence on an equal footing in a single framework. It is important for VMC results to benchmark the accuracy by comparing with the available accurate results obtained without assuming biased forms of wave functions as those listed in the second column. By comparing with established results, we show in Appendices B and G that our wave functions allow precise estimations of physical properties.

In the fifth column, the results of VMC and CPMC methods, which mainly study the normal state properties and instability toward PS, are shown. Neuscamman *et al*. [23] used a variational wave function with a large number of variational parameters, which is similar to our model. However, their estimate of the phase separation region in the doped Hubbard model extends to a larger doping concentration $\delta \sim 0.15$, even at $U/t = 4$. This contradicts other previous and the present estimates. The reason for the overestimation of the phase separation in Ref. [23] is unclear for now. The CPMC studies also suggest a phase separation up to $\delta \sim 0.1$ at $U/t = 4$ [21] (or incommensurate antiferromagnetic order instead [48]). This has been criticized in Ref. [22] by taking into account the coexisting antiferromagnetic and BCS guiding functions, which give, more or less, the absence of the phase separation. Many works, including those using numerically exact methods such as QMC, suggest that PS does not occur in the weak-coupling region ($U/t \lesssim 8$) and our present work is consistent with them. Although Becca *et al*. [49] claim that PS does not occur even in the strong-coupling region ($U/t = 10$) due to the charge structure factor by using Green's-function Monte Carlo (GFMC) method, the charge structure factor is not a proper quantity to detect the PS, as we show in Appendix E. For the case with the next-neighbor hopping $t' = -0.4t$, the phase separation is observed at strong coupling $U/t = 10$ [25].

Our result on the PS is consistent with most of the former studies where the PS occurs in the strong-coupling region. However, the relation between the PS and superconductivity, clarified as a key in the present work, has not been well studied in the literature.

Here we discuss the previous studies on the extended Hubbard model. In the strong-coupling region, the effects of intersite interactions such as V/t and J/t are studied by using VMC and CDMFT [56,57]. They showed that the intersite Coulomb interaction V reduces the superconducting order parameter; however, they do not study the competitions with other phases such as the antiferromagnetic phase.

Thus, it is not clear whether the superconducting phase is robust against intersite Coulomb interactions. By performing calculations that treat the superconducting phase and the antiferromagnetic phase or strongly correlated metal on an equal footing, we show that the superconducting phase becomes unstable for small V ($V/U = 0.1$). This fragility of the superconducting phase is not clarified in previous studies.

In addition, we again note that the CDMFT often overestimates the stability of the superconducting phase because of its mean-field nature.

APPENDIX B: BENCHMARK OF THE PRESENT MVMC METHOD

To show the accuracy of the present mVMC method, we compare our results with those of the exact diagonalization (ED), auxiliary-field QMC, and GBMC for the Hubbard model

TABLE II. [$U/t = 4$] Comparison of energy, peak value of spin structure $S(\boldsymbol{q}_{\rm peak})/N_{\rm s}$, its wave number $\boldsymbol{q}_{\rm peak}$, and nearest-neighbor spin correlation $\langle \boldsymbol{S}_i \cdot \boldsymbol{S}_j \rangle$ between the exact diagonalization (ED) results and those of mVMC, where mVMC(2×2) means that the number of the variational parameters for f_{ij} is $2 \times 2 \times N_s$. The parentheses denote the error bars in the last digit.

Physical properties	mVMC(2×2)	ED
4×4(PP), $n = 1$		
Energy per site	−0.8500(1)	−0.8513
$S(\boldsymbol{q}_{\rm peak})/N_{\rm s}$	0.0575(2)	0.0569
$\boldsymbol{q}_{\rm peak}$	(π,π)	(π,π)
$\langle \boldsymbol{S}_i \cdot \boldsymbol{S}_j \rangle$	−0.2063(14)	−0.2063
4×4(PP), $n = 0.625$		
Energy per site	−1.2196(1)	−1.22380
$S(\boldsymbol{q}_{\rm peak})/N_{\rm s}$	0.0130(1)	0.01300
$\boldsymbol{q}_{\rm peak}$	$(\pi/2,\pi)$	$(\pi/2,\pi)$
$\langle \boldsymbol{S}_i \cdot \boldsymbol{S}_j \rangle$	−0.0704(5)	−0.0683
4×4(AP), $n = 1$		
Energy per site	−0.9081(1)	−0.9120
$S(\boldsymbol{q}_{\rm peak})/N_{\rm s}$	0.0414(1)	0.039698
$\boldsymbol{q}_{\rm peak}$	(π,π)	(π,π)
$\langle \boldsymbol{S}_i \cdot \boldsymbol{S}_j \rangle$	−0.1591(8)	−0.1537
4×4(AP), $n = 0.75$		
Energy per site	−1.1504(1)	−1.1607
$S(\boldsymbol{q}_{\rm peak})/N_{\rm s}$	0.0179(2)	0.0179
$\boldsymbol{q}_{\rm peak}$	$(\pi,0)$	$(\pi,\pi/2)$
$\langle \boldsymbol{S}_i \cdot \boldsymbol{S}_j \rangle$	−0.0944(7)	−0.0936

on the square lattice, since they generally provide us with the best estimates of the energy, as well as other physical properties. A weak point of the QMC and GBMC methods is that they are applicable only in the region up to the intermediate coupling. However, they give accurate energies and physical properties and are useful for the benchmark. In fact, the QMC is a numerically exact method within the statistical error, and the GBMC is well established to give very good agreement with the QMC and ED results in the range $U \leqslant 6$ [5].

In Tables II and III, we show the results of mVMC and ED at half filling as well as the doped case for $U/t = 4$ and $U/t = 10$. To see the boundary effects, we calculate both PP and AP boundary conditions. For the doped case, we choose the closed-shell filling for PP and AP boundary conditions. The total energy is well consistent with the values of ED, and the relative errors, $\delta E = 1 - E_{\rm mVMC}/E_{\rm ED}$, are typically less than 1%, even for the strong-coupling regime ($U/t = 10$). Peak values of the spin structure factor are also well consistent with the exact values in all the cases. We also confirm that nearest-neighbor spin correlations $\langle \boldsymbol{S}_i \cdot \boldsymbol{S}_j \rangle$ are well consistent with the results of ED.

We also perform the first- and second-step power Lanczos method for $U/t = 4$ at half filling. In Fig. 7, we plot the energy as a function of the variance, which is defined as $\Delta_{\rm var} = (\langle H^2 \rangle - \langle H \rangle^2)/\langle H \rangle^2$. As shown in Fig. 7, the power Lanczos steps systematically improve the energies. Since the energy difference from the exact ground-state energy is linearly

TABLE III. [$U/t = 10$] Comparison of energy, peak value of spin structure $S(\boldsymbol{q}_{\rm peak})/N_{\rm s}$, its wave number $\boldsymbol{q}_{\rm peak}$, and nearest-neighbor spin correlation $\langle \boldsymbol{S}_i \cdot \boldsymbol{S}_j \rangle$. The method is the same as Table II. The parentheses denote the error bars in the last digit.

Physical properties	mVMC(2×2)	ED
4×4(PP), $n = 1$		
Energy per site	−0.43632(5)	−0.43931
$S(\boldsymbol{q}_{\rm peak})/N_{\rm s}$	0.0860(3)	0.0835
$\boldsymbol{q}_{\rm peak}$	(π,π)	(π,π)
$\langle \boldsymbol{S}_i \cdot \boldsymbol{S}_j \rangle$	−0.3010(9)	−0.3057
4×4(PP), $n = 0.625$		
Energy per site	−1.0444(3)	−1.0564
$S(\boldsymbol{q}_{\rm peak})/N_{\rm s}$	0.01505(7)	0.01508
$\boldsymbol{q}_{\rm peak}$	$(\pi/2,\pi)$	$(\pi/2,\pi)$
$\langle \boldsymbol{S}_i \cdot \boldsymbol{S}_j \rangle$	−0.0818(5)	−0.0754
4×4(AP), $n = 1$		
Energy per site	−0.4422(1)	−0.4457
$S(\boldsymbol{q}_{\rm peak})/N_{\rm s}$	0.0852(2)	0.0819
$\boldsymbol{q}_{\rm peak}$	(π,π)	(π,π)
$\langle \boldsymbol{S}_i \cdot \boldsymbol{S}_j \rangle$	−0.2994(17)	−0.3044
4×4(AP), $n = 0.75$		
Energy per site	−0.9022(3)	−0.9255
$S(\boldsymbol{q}_{\rm peak})/N_{\rm s}$	0.0261(3)	0.0216
$\boldsymbol{q}_{\rm peak}$	$(\pi,0)$	$(\pi,\pi/2)$
$\langle \boldsymbol{S}_i \cdot \boldsymbol{S}_j \rangle$	−0.1087(15)	−0.1073

proportional to $\Delta_{\rm var}$ for sufficiently small variance [35], we can estimate more precise ground-state energy by performing the linear fitting of the energies as a function of $\Delta_{\rm var}$. Since the studies with the Lanczos step require substantially heavier computational costs and the physical quantities change little after the Lanczos step, as in Figs. 1 and 19, we have performed the Lanczos calculation only for a small number of examples, which is sufficient to confirm the validity of the result. Systematic studies of the effects of further power Lanczos steps are beyond the scope of this paper and are left for future studies.

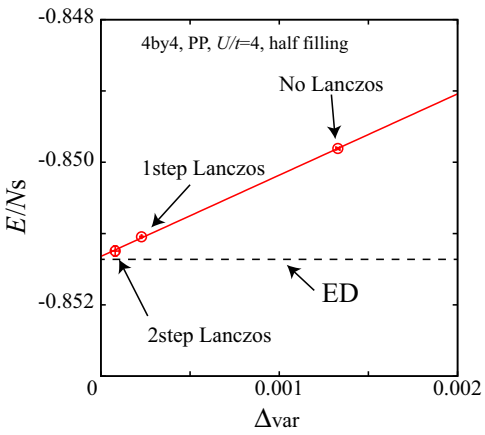

FIG. 7. (Color online) Variance $\Delta_{\rm var}$ dependence of energies for zero-, first-, and second-step power Lanczos calculations. Solid line represents the result of linear fitting of energies. We employ the PP boundary condition.

TABLE IV. Comparison of total energy between mVMC results and those of numerically well-benchmarked accurate methods. The parentheses denote the error bars in the last digit.

	QMC	GBMC	mVMC
8×8 (PP), $n = 50/64$			
$U/t = 4$	$-72.80(6)$	$-72.51(5)$	$-71.417(4)$
$U/t = 6$		$-63.64(12)$	$-62.553(9)$
10×10 (PP), $n = 82/100$			
$U/t = 4$	$-109.7(6)$		$-107.51(1)$
$U/t = 6$		$-92.07(22)$	$-91.91(1)$
12×12 (PP), $n = 122/144$			
$U/t = 4$	$-151.4(14)$		$-150.14(2)$

In Table IV, we compare the results of mVMC with available QMC and GBMC at different fillings for $U/t = 4$ and $U/t = 6$. The PP boundary condition is employed. In large systems, our mVMC offers consistent results with the QMC and GBMC calculations. These results also confirm the accuracy of our mVMC method. We also note that the accuracy of the GBMC compared with the available QMC results has well been benchmarked in physical properties, including the superconducting correlations [5].

In Figs. 8 and 9, we show the pairing correlations $P_{d_{x^2-y^2}}(r)$ calculated by mVMC and ED for the doped case. Our mVMC method well reproduces the exact superconducting correlation for all the distances. We note that the deviation from the exact value is large for $U/t = 10$ at $r = \sqrt{2}$ in Fig. 8. This deviation of the short-range part is not significant because the long-range part of $P_{d_{x^2-y^2}}(r)$ is essential to detect the appearance of the superconducting phase. For larger system sizes ($N_s = 8 \times 8$), we compare the pairing correlations obtained by mVMC with those by GBMC. As shown in Fig. 10, our mVMC method well reproduces the exact superconducting correlation for all the distances.

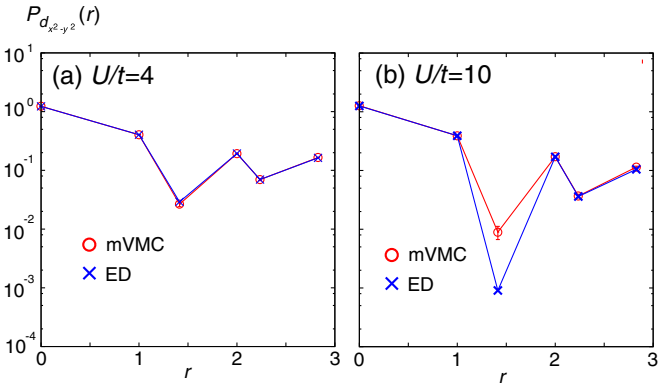

FIG. 8. (Color online) Distance dependence of $d_{x^2-y^2}$-wave superconducting correlation $P_{d_{x^2-y^2}}(r)$ at $n = 10/16 = 0.625$ for PP boundary condition. For $U/t = 4$ and $U/t = 10$, mVMC well reproduces the exact values. In the present plots and the plots in the later figures, the error bars indicate the estimated statistical errors of the Monte Carlo sampling (see Sec. II).

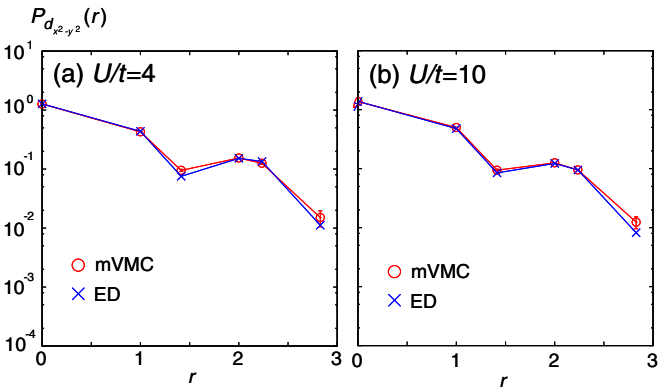

FIG. 9. (Color online) Superconducting correlation $P_{d_{x^2-y^2}}(r)$ for $d_{x^2-y^2}$-wave symmetry as a function of distance r at $n = 12/16 = 0.75$ for 4×4 lattice with the AP boundary condition. For both $U/t = 4$ and $U/t = 10$, mVMC well reproduces the exact values (ED).

We also show doping dependence of the spin structure factor $S(\boldsymbol{q}_{\rm peak})$ for $U/t = 4$ in Fig. 11. Our mVMC well reproduces the QMC results. The accuracy and applicability of the mVMC method in general have also been examined in the literature [32,58–60].

APPENDIX C: DETAILS OF CONDENSATION ENERGY

In this section we show the details of condensation energy, i.e., kinetic-energy gain $\Delta E_{\rm kin}$ and potential-energy gain ΔE_U, which are defined as

$$\begin{aligned} E_{\rm kin} &= -t \sum_{\langle i,j \rangle} \langle c^\dagger_{i\sigma} c_{j\sigma} + \text{H.c.} \rangle, \\ E_U &= U \sum_i \langle n_{i\uparrow} n_{i\downarrow} \rangle, \\ \Delta E_{\rm kin} &= (E_{\rm kin,SC} - E_{\rm kin,Normal})/N_s, \\ \Delta E_U &= (E_{U,\rm SC} - E_{U,\rm Normal})/N_s. \end{aligned} \tag{C1}$$

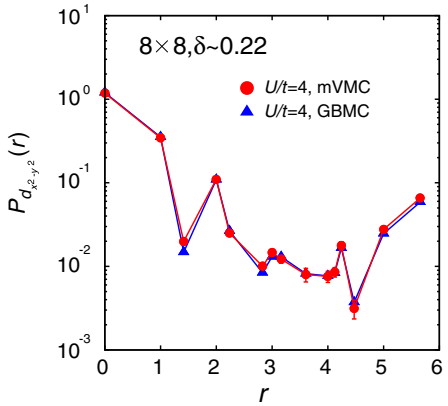

FIG. 10. (Color online) Superconducting correlation $P_{d_{x^2-y^2}}(r)$ for $d_{x^2-y^2}$-wave symmetry as a function of distance r for $\delta = 1 - 50/64 \sim 0.22$ and $U/t = 4$ at $N_s = 8 \times 8$ (PP boundary condition). It is confirmed that mVMC well reproduces the essentially exact results of GBMC.

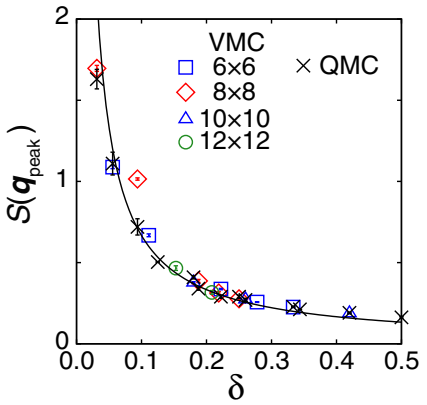

FIG. 11. (Color online) Doping dependence of spin structure factor $S(\boldsymbol{q}_{\rm peak})$ for $U/t = 4$ and several different system sizes (PP boundary condition). QMC results [4] are shown by black crosses. Black solid line is a guide for the eyes.

We also show the nearest-neighbor spin correlation ΔS, which is defined as

$$S_{\rm nn} = \langle \boldsymbol{S}_i \cdot \boldsymbol{S}_j \rangle,$$
$$\Delta S = (S_{\rm nn,SC} - S_{\rm nn,Normal}), \tag{C2}$$

where i and j represent the nearest-neighbor sites.

In Fig. 12 we show the doping dependence of $\Delta E_{\rm kin}$ and ΔE_U for several choices of parameters. In the simple Hubbard model, i.e., without V and J, the superconducting phase is stabilized by the energy gain of the potential energy in the entire doping region. By introducing V and J, the energy gain of the potential energy becomes large while the energy loss of kinetic energy also becomes large. This is because stronger pairing disturbs the single-particle motion and at the same time the d-wave pairing strictly excludes the double occupation of the paired electron by symmetry, which contributes to the gain in the interaction energy and the loss in the kinetic energy. It was claimed that the kinetic-energy gain exists in the strong-coupling region [12,47]. However, this gain was calculated in the superconducting state without the antiferromagnetic order or correlations, while in reality the superconducting phase largely coexists with the antiferromagnetic order or at least with its well developed short-range correlations in the ground state. This coexistence leads to a large gain in the interaction energy and a loss in the kinetic energy in the superconducting state in comparison to the state with the antiferromagnetic correlations only. Because the energy gain arising from the short-range singlet correlation exists for finite J, total condensation energy becomes large compared to the simple Hubbard model. As shown in Fig. 13, short-range singlet correlation does not largely depend on interaction parameters.

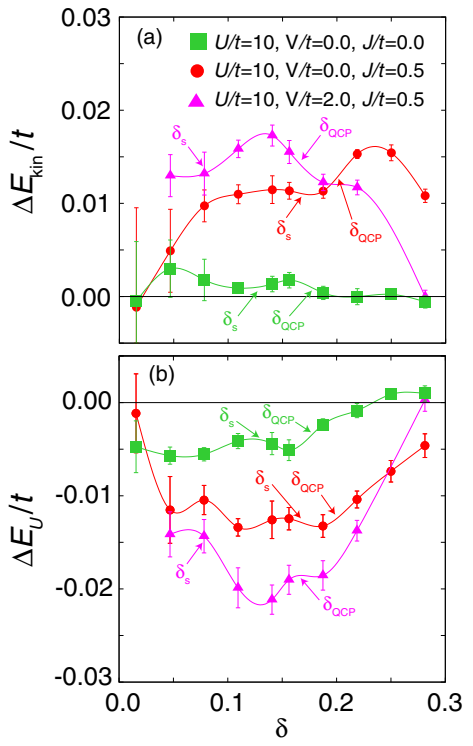

FIG. 12. (Color online) Doping dependence of kinetic- and potential-energy gains in superconducting phase.

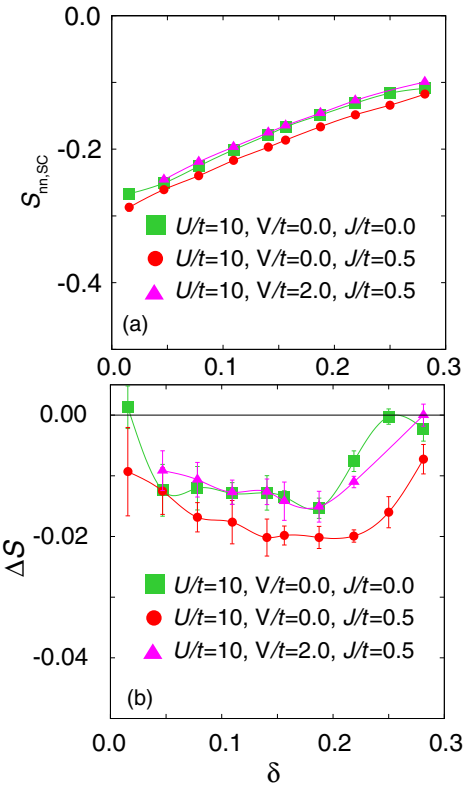

FIG. 13. (Color online) Doping dependence of (a) nearest-neighbor spin correlations in superconducting phase ($S_{\rm nn,SC}$) and (b) $\Delta S = S_{\rm nn,SC} - S_{\rm nn,Normal}$.

In Fig. 14 we show the kinetic (potential) part of chemical potential $\mu_{\rm kin}$ (μ_U) for $U/t = 10$, defined as

$$\mu_{\rm kin}(\bar{N}) = \{E_{\rm kin}(N_1) - E_{\rm kin}(N_2)\}/\{N_1 - N_2\},$$
$$\mu_U(\bar{N}) = \{E_U(N_1) - E_U(N_2)\}/\{N_1 - N_2\} - \frac{U}{2},$$

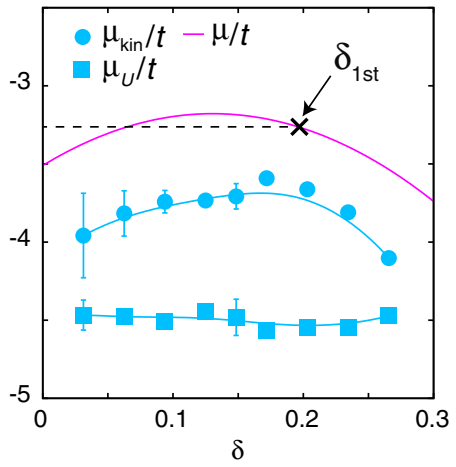

FIG. 14. (Color online) Doping dependence of kinetic (potential) part of chemical potential $\mu_{\rm kin}$ (μ_U) for $U/t = 10$ and $N_{\rm s} = 16 \times 16$. Solid lines are guides for the eyes. We also show total chemical potential μ for $U/t = 10$, which is the same one as shown in Fig. 3 in the main text. Black dashed line represents the line that is used for Maxwell's construction. For comparison, we shift $\mu_{\rm kin}$ by $-U/2$.

where $\bar{N} = \{N_1 + N_2\}/2$. The kinetic part of the chemical potential shows the convex doping dependence, while μ_U is nearly independent of the doping. This convex doping dependence of $\mu_{\rm kin}$ suggests that PS is mainly caused by the kinetic energy.

A strong crossover from the states with Mott proximity in the underdoped region to the overdoped region takes place in a twofold way: the charge instability represented by divergence of charge compressibility at $\delta = \delta_{\rm s}$, and the magnetic instability represented by divergence of antiferromagnetic susceptibility at $\delta = \delta_{\rm QCP}$. This "soft" fluctuating region provides the grounds for the gain in the condensation energy.

APPENDIX D: RESULTS WITH NEXT-NEAREST-NEIGHBOR HOPPING $t' = -0.3t$

In this section we examine the effects of next-nearest-neighbor hopping. To directly compare with the case of $t'/t = 0$, we employ the same on-site Coulomb repulsion, i.e., $U/t = 10$. When the next-nearest-neighbor hopping $t' = -0.3t$ is present following the realistic parameter of the cuprate superconductors, the condensation energy is strongly suppressed, as we see in Fig. 15(a). Concomitantly with this suppression, the phase separation also disappears, as we see Fig. 16. The antiferromagnetically ordered region changes little, as we see in Fig. 15(b). The results are not well consistent with the experimental results of the hole-doped copper oxides expected from the material dependence of the parameters in the following points: (1) The suppression of the superconductivity at larger $-t'/t$ does not follow the relation between the expected material dependence of t'/t and the critical temperature T_c [61]. (2) A wide antiferromagnetically ordered region is not consistent with quick destruction of the antiferromagnetic order upon hole doping. The origin of the discrepancy is unclear at the moment. Possible origins are

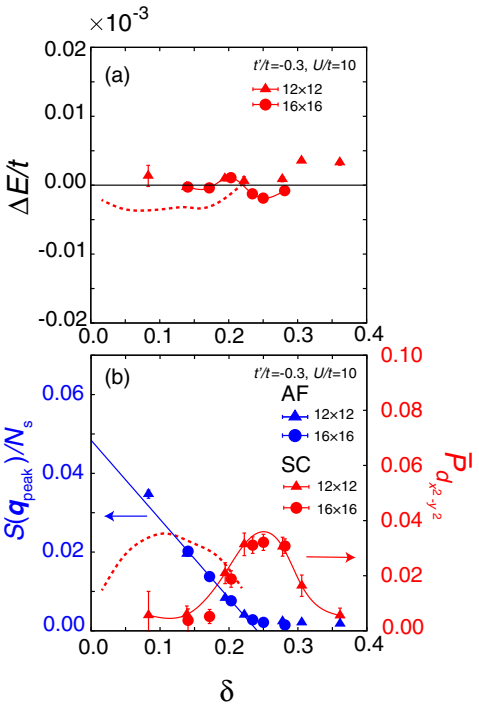

FIG. 15. (Color online) (a) Doping dependence of condensation energy ΔE for $U/t = 10, t'/t = -0.3$. Broken red line represents the condensation energy for $U/t = 10, t'/t = 0$. (b) Doping (δ) dependence of averaged $d_{x^2-y^2}$-wave superconducting correlations $\bar{P}_{x^2-y^2}$ and peak values of spin structure factors $S(\boldsymbol{q}_{\rm peak})$ for $U/t = 10$ and $t'/t = -0.3$. For comparison, we plot $\bar{P}_{x^2-y^2}$ of $U/t = 10, t'/t = 0$ by the broken line.

the following: (1) A realistic value of the on-site Coulomb repulsion is smaller than the present value $U/t = 10$. (2) A combination of V and J expected in the effective low-energy model is required to stabilize the superconductivity. (3) Single-band models are not sufficient to reproduce the quantitative aspect of the copper oxides. (4) Small but finite impurities immediately destroy the antiferromagnetic order.

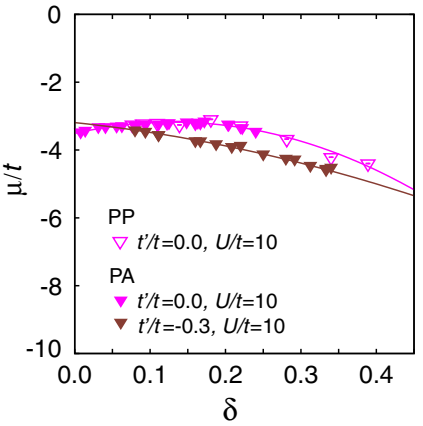

FIG. 16. (Color online) Doping dependence of chemical potential μ for $t'/t = 0$ and $t'/t = -0.3$.

APPENDIX E: AMPLITUDE OF CHARGE STRUCTURE FACTOR IN MACROSCOPIC PHASE-SEPARATED PHASE

In this section, we estimate the amplitude of the charge structure factor allowed in finite-size systems when the phase separation occurs as a macroscopic phase. In the canonical ensemble, the charge structure factor, $N(\boldsymbol{q}) = \frac{1}{N_s}\sum_{i,j}\langle n_i n_j\rangle e^{i\boldsymbol{q}\cdot(\boldsymbol{r}_i-\boldsymbol{r}_j)}$, at $\boldsymbol{q}=0$ must be zero because total charge should be conserved, while one may expect the growth of $N(\boldsymbol{q})$ at the lowest possible wave number as the signature of the Bragg peak at $\boldsymbol{q}=0$, expected for the phase separation region. However, here we show that the growth is in practice suppressed by the energy loss caused by the domain wall formation in numerically accessible system sizes.

We first roughly estimate the energy cost caused by the density modulation imposed in a metal with the period of system size (namely, at the nonzero and lowest possible wave number in the periodic boundary condition) necessary to simulate the energy cost by the domain wall formation between two different density phases. (Note that this estimate is valid if the density modulation from the uniform phase is small, which is justified later.) For this purpose, we consider the noninteracting Hamiltonian $H_0 = \sum_{\boldsymbol{k},\sigma}\epsilon_{\boldsymbol{k}} c^\dagger_{\boldsymbol{k}\sigma} c_{\boldsymbol{k}\sigma}$, where $\boldsymbol{k}$ is the momentum vector and $\epsilon_{\boldsymbol{k}}$ is band dispersion, respectively. The ground state of this Hamiltonian is a Fermi-sea state (with of course uniform density), which is defined as $|\phi_0\rangle = \prod_{|\boldsymbol{k}|<k_F,\sigma} c^\dagger_{\boldsymbol{k}\sigma}|0\rangle$, where k_F is Fermi wave number. Here we calculate the energy loss in the charge-modulated (CM) phase $|\phi_{\rm CM}\rangle$, which is defined as

$$\begin{aligned} |\phi_{\rm CM}\rangle &= \hat{\rho}|\phi_0\rangle, \\ \hat{\rho} &= 1+\gamma\hat{n}_{\boldsymbol{q}}, \\ \hat{n}_{\boldsymbol{q}} &= \sum_{\boldsymbol{r}_i,\sigma} c^\dagger_{\boldsymbol{r}_i\sigma} c_{\boldsymbol{r}_i\sigma} e^{i\boldsymbol{q}\boldsymbol{r}_i} = \sum_{\boldsymbol{k}} c^\dagger_{\boldsymbol{k}+\boldsymbol{q}\sigma} c_{\boldsymbol{k}\sigma}, \end{aligned} \tag{E1}$$

where $\boldsymbol{q}$ is the wave number of charge modulation. For simplicity, we consider a square lattice [$\epsilon_{\boldsymbol{k}} = -2t^*(\cos k_x + \cos k_y)$], $\boldsymbol{q} = (q_x = 2\pi/L, 0)$ (L is the linear dimension of system), and half filling [see Fig. 17(a)]. Note that $\boldsymbol{q}$ is the lowest possible wave number of the density modulation. First, we calculate the local density at site l as follows:

$$\begin{aligned} \langle c^\dagger_{l\sigma} c_{l\sigma}\rangle &= \frac{\langle\phi_{\rm CM}|c^\dagger_{l\sigma}c_{l\sigma}|\phi_{\rm CM}\rangle}{\langle\phi_{\rm CM}|\phi_{\rm CM}\rangle} \\ &= \frac{N_e}{2N_s} + \frac{2\gamma}{L}\frac{\cos\frac{2\pi l}{L}}{1+M|\gamma|^2}, \end{aligned} \tag{E2}$$

where N_e is number of total electrons and $M = \langle\phi_0|\hat{n}^\dagger_{\boldsymbol{q}}\hat{n}_{\boldsymbol{q}}|\phi_0\rangle = \sum_{\boldsymbol{k}\in R,\sigma} \sim 2L$ [definition of R, see Fig. 17(a)]. Therefore, by assuming $M|\gamma|^2 \ll 1$, the amplitude of charge modulation η is approximately given as

$$\eta \sim 2\times\frac{2\gamma}{L}, \tag{E3}$$

where factor 2 comes from the spin degrees of freedom. Here we define mean charge modulation $\bar{\eta}$ as

$$\bar{\eta} = \frac{1}{L}\times\int_0^L \eta\left|\cos\frac{2\pi}{L}x\right|dx = \frac{2}{\pi}\eta. \tag{E4}$$

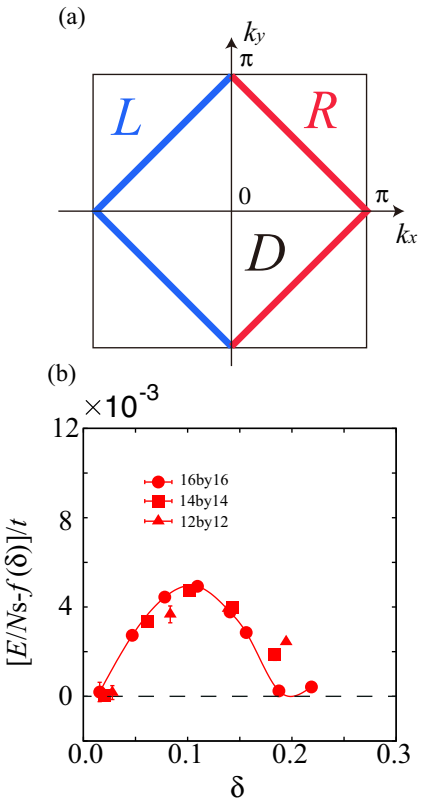

FIG. 17. (Color online) (a) Schematic picture of Fermi surface (red and blue thick line). Region D denotes the inside of the Fermi surface and $R(L)$ denotes the right (left) edge of the Fermi surface, respectively. (b) Doping dependence of the total energy for $U/t = 10, V = J = 0$ for several system sizes. AP boundary condition is used. For clarity, we subtract $f(\delta)$, which is a linear function of δ. The solid line is a guide for the eyes. From this, we estimate the energy gain of phase separation as $\Delta E_{\rm PS} = 0.5\times10^{-3}t\times\delta/0.1$, when the density difference of the phase-separated two phases is 2δ.

Then the energy loss within the first order with respect to $\boldsymbol{q}$ is calculated as follows:

$$\begin{aligned} E_{\boldsymbol{q}} &= \frac{\langle\phi_{\rm CM}|H_0|\phi_{\rm CM}\rangle}{\langle\phi_{\rm CM}|\phi_{\rm CM}\rangle} \\ &= \sum_{\boldsymbol{k}\in D,\sigma}\epsilon_{\boldsymbol{k}} + \frac{|\gamma|^2}{1+M|\gamma|^2}\left[-\sum_{\boldsymbol{k}\in R,\sigma}\epsilon_{\boldsymbol{k}} + \sum_{\boldsymbol{k}\in R,\sigma}\epsilon_{\boldsymbol{k}+\boldsymbol{q}}\right] \\ &\sim \sum_{\boldsymbol{k}\in D,\sigma}\epsilon_{\boldsymbol{k}} + \frac{|\gamma|^2 q_x}{1+M|\gamma|^2}\sum_{\boldsymbol{k}\in R,\sigma}\frac{\partial\epsilon_{\boldsymbol{k}}}{\partial k_x}. \end{aligned} \tag{E5}$$

From this, we evaluate the energy loss arising from the density modulation $\Delta E_{\rm CM}$ as

$$\begin{aligned} \Delta E_{\rm CM} &\equiv E_{\boldsymbol{q}} - E_{\boldsymbol{q}=\boldsymbol{0}} \\ &= \frac{|\gamma|^2 q_x}{1+M|\gamma|^2}\sum_{\boldsymbol{k}\in R,\sigma} 2t^*\sin k_x \\ &\sim 16|\gamma|^2 t^*, \end{aligned} \tag{E6}$$

where we again assume $M|\gamma|^2 \ll 1$.

If the energy loss $\Delta E_{\rm CM}$ is smaller than the energy gain of the phase separation $\Delta E_{\rm PS}$, the spatially inhomogeneous phase

becomes stable. As shown in Fig. 17(b), from the mVMC calculations for a typical case ($U/t = 10, V = J = 0$), we determine that the energy gain by the phase separation with the amplitude 0.1 (in the unit of the doping concentration δ) is at most $5 \times 10^{-3}t$. Then we have roughly estimated the energy gain in the case of the density modulation $\bar{\eta}$ as $5 \times 10^{-3}t \times \bar{\eta}/0.1$, simply by approximating the curve in Fig. 17(b) by a linear function. Thus, the condition that the spatially inhomogeneous phase becomes stable is given by

$$\frac{\Delta E_{\mathrm{CM}}}{N_{\mathrm{s}}} \sim \frac{16|\gamma|^2 t^*}{N_{\mathrm{s}}} < \Delta E_{\mathrm{PS}} \sim 5 \times 10^{-3} t \times \frac{\bar{\eta}}{0.1}. \quad \text{(E7)}$$

Given that this condition is satisfied and by assuming that t^* is the same as t, we can evaluate the maximally allowed amplitude of the charge modulation as

$$|\eta| < 0.03 \quad \text{(E8)}$$

in finite-size systems. Thus, even when the phase separation is the correct solution in the infinite-size system, the amplitude of charge structure factor $N(\boldsymbol{q})$ at the lowest possible wave number for $N_{\mathrm{s}} = 16 \times 16 = 256$ is given as

$$N(\boldsymbol{q}) = \frac{1}{N_{\mathrm{s}}} \sum_{i,j} n_i n_j e^{i\boldsymbol{q}(\boldsymbol{r}_i - \boldsymbol{r}_j)} = N_{\mathrm{s}} \times |\eta|^2 \sim 0.2. \quad \text{(E9)}$$

Although the present estimate is rough, the order estimate of enhancement is expected to be correct. Around $\boldsymbol{q} \sim 0$, we indeed see $N(\boldsymbol{q})$ in the order of 0.1, as shown in Fig. 18, but it is buried in the background structure. Thus, it is difficult to see a clear signature of the phase separation from $N(\boldsymbol{q})$ in the available system size. In contrast to this, the doping dependence of the chemical potential μ offers a reliable estimation of the phase separation region in relatively small systems, because they can be correctly calculated by the uniform density state. Further analysis, such as performing calculations for larger system sizes, is an intriguing issue but left for future study.

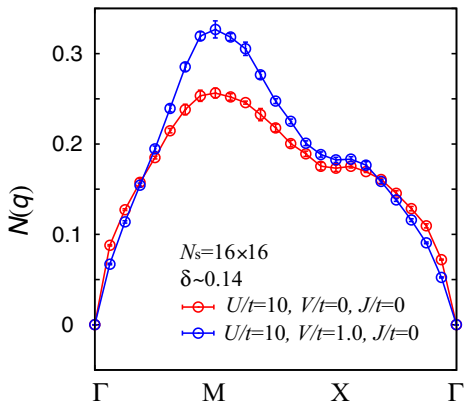

FIG. 18. (Color online) Momentum dependence of the charge structure factor $N(\boldsymbol{q})$ at $\delta \sim 0.14$ for $U/t = 10, V/t = 0, J/t = 0$ and $U/t = 10, V/t = 1.0, J/t = 0$. The system size is $N_{\mathrm{s}} = 16 \times 16$, and the AP boundary condition is employed.

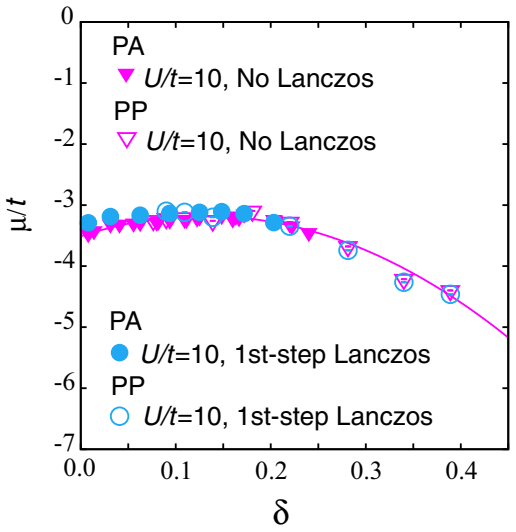

FIG. 19. (Color online) Doping dependence of chemical potential μ for $U/t = 10$ after the first power Lanczos step. For comparison, we show the doping dependence of μ for no Lanczos step.

APPENDIX F: DOPING DEPENDENCE OF CHEMICAL POTENTIAL AFTER LANCZOS STEP

Here we show how the Lanczos step affects the doping dependence of the chemical potential μ. In Fig. 19, we show the doping dependence μ after the first Lanczos step for $U/t = 10$ and $J = V = 0$. From this, although the Lanczos step largely improves the energies, we find that it changes the doping dependence of μ little, which is defined by the difference of the energies for different δ values [see Eq. (4)]. At this stage, due to the heavy numerical cost, we cannot perform the further Lanczos calculation and systematic variance extrapolation. Thus, precise estimation of the phase separation region by systematic power Lanczos calculation is left for future study.

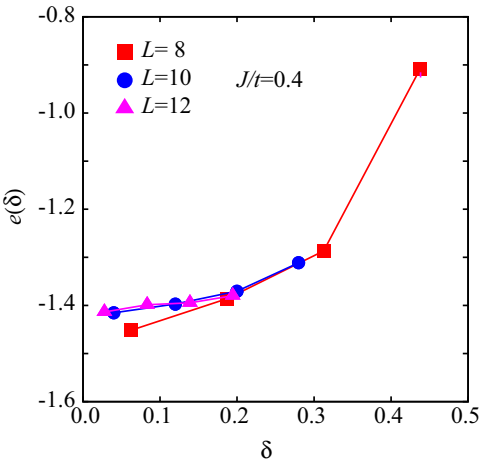

FIG. 20. (Color online) Doping dependence of $e(\delta)$ for $J/t = 0.4$. We employ antiperiodic-periodic boundary conditions. Since $e(\delta)$ increases monotonically, the absence of PS is concluded [62].

APPENDIX G: BENCHMARK RESULTS FOR THE t-J MODEL

The t-J model on the square lattice is defined as

$$H = -t \sum_{\langle i,j\rangle,\sigma} (c^{\dagger}_{i\sigma} c_{j\sigma} + \text{H.c.}) + J \sum_{\langle i,j\rangle} \left(\boldsymbol{S}_i \cdot \boldsymbol{S}_j - \frac{1}{4} n_i n_j \right),$$

where the double occupancy is completely prohibited. In the t-J model, it is suggested that the phase separation does not occur for sufficiently small J [62]. To benchmark the accuracy of our variational wave function, we perform the calculations for the t-J model at $J/t = 0.4$. We use basically the same wave function defined in Eq. (1), except that we completely prohibit double occupancy by using the Gutzwiller factors. We note that the doublon-holon correlation factors are omitted. We plot $e(\delta) = [E(\delta)/N_s - E(0)/N_s]/\delta$ in Fig. 20, which can be directly compared with Fig. 1 in Ref. [62]. Although values of $e(\delta)$ themselves are slightly different from those in Ref. [62], our calculation supports the absence of the PS consistently with Ref. [62]. In the Heisenberg limit ($\delta = 0$), we compare our result with the quantum Monte Carlo method [63] and we obtain $|1 - E_{\text{mVMC}}/E_{\text{QMC}}| \sim 0.002$ for $N_s = 12 \times 12$. This result again confirms that our variational wave function has sufficient accuracy to discuss the existence of PS.

[1] J. G. Bednorz and K. A. Müller, Z. Phys. **64**, 189 (1986).
[2] H. Mukuda, Y. Yamaguchi, S. Shimizu, Y. Kitaoka, P. Shirage, and A. Iyo, J. Phys. Soc. Jpn. **77**, 124706 (2008).
[3] J. Wu, O. Pelleg, G. Logvenov, A. T. Bollinger, Y.-J. Sun, G. S. Boebinger, M. Vanetić, Z. Radović, and I. Božović, Nature Mater. **12**, 877 (2013).
[4] N. Furukawa and M. Imada, J. Phys. Soc. Jpn. **61**, 3331 (1992).
[5] T. Aimi and M. Imada, J. Phys. Soc. Jpn. **76**, 113708 (2007).
[6] H. Yokoyama, M. Ogata, Y. Tanaka, K. Kobayashi, and H. Tsuchiura, J. Phys. Soc. Jpn. **82**, 014707 (2013).
[7] T. A. Maier, M. Jarrell, T. C. Schulthess, P. R. C. Kent, and J. B. White, Phys. Rev. Lett. **95**, 237001 (2005).
[8] M. Aichhorn, E. Arrigoni, M. Potthoff, and W. Hanke, Phys. Rev. B **76**, 224509 (2007).
[9] E. Khatami, K. Mikelsons, D. Galanakis, A. Macridin, J. Moreno, R. T. Scalettar, and M. Jarrell, Phys. Rev. B **81**, 201101(R) (2010).
[10] M. Capone and G. Kotliar, Phys. Rev. B **74**, 054513 (2006).
[11] G. Sordi, P. Sémon, K. Haule, and A.-M. S. Tremblay, Phys. Rev. Lett. **108**, 216401 (2012).
[12] E. Gull and A. J. Millis, Phys. Rev. B **86**, 241106 (2012).
[13] K.-S. Chen, Z. Y. Meng, S.-X. Yang, T. Pruschke, J. Moreno, and M. Jarrell, Phys. Rev. B **88**, 245110 (2013).
[14] T. Moriya and K. Ueda, Rep. Prog. Phys. **66**, 1299 (2003).
[15] D. Eichenberger and D. Baeriswyl, Phys. Rev. B **79**, 100510 (2009).
[16] S. Zhang, J. Carlson, and J. E. Gubernatis, Phys. Rev. Lett. **78**, 4486 (1997).
[17] W. Metzner, M. Salmhofer, C. Honerkamp, V. Meden, and K. Schönhammer, Rev. Mod. Phys. **84**, 299 (2012).
[18] P. A. Lee, N. Nagaosa, and X.-G. Wen, Rev. Mod. Phys. **78**, 17 (2006).
[19] V. J. Emery, S. A. Kivelson, and H. Q. Lin, Phys. Rev. Lett. **64**, 475 (1990).
[20] S. A. Kivelson, E. Fradkin, and V. J. Emery, Nature (London) **393**, 550 (1998).
[21] C.-C. Chang and S. Zhang, Phys. Rev. B **78**, 165101 (2008).
[22] S. Sorella, Phys. Rev. B **84**, 241110 (2011).
[23] E. Neuscamman, C. J. Umrigar, and Garnet Kin-Lic Chan, Phys. Rev. B **85**, 045103 (2012).
[24] S. R. White and D. J. Scalapino, Phys. Rev. Lett. **80**, 1272 (1998).
[25] L. F. Tocchio, H. Lee, H. O. Jeschke, R. Valentí, and C. Gros, Phys. Rev. B **87**, 045111 (2013).
[26] M. Imada, Phys. Rev. B **72**, 075113 (2005).
[27] M. Imada, J. Phys. Soc. Jpn. **74**, 859 (2005).
[28] M. C. Gutzwiller, Phys. Rev. Lett. **10**, 159 (1963).
[29] R. Jastrow, Phys. Rev. **98**, 1479 (1955).
[30] M. Capello, F. Becca, M. Fabrizio, S. Sorella, and E. Tosatti, Phys. Rev. Lett. **94**, 026406 (2005).
[31] H. Yokoyama and H. Shiba, J. Phys. Soc. Jpn. **59**, 3669 (1990).
[32] D. Tahara and M. Imada, J. Phys. Soc. Jpn. **77**, 114701 (2008).
[33] C. Gros, Ann. Phys. **189**, 53 (1989).
[34] M. Bajdich, L. Mitas, L. K. Wagner, and K. E. Schmidt, Phys. Rev. B **77**, 115112 (2008).
[35] S. Sorella, Phys. Rev. B **64**, 024512 (2001).
[36] E. Heeb and T. Rice, Z. Phys. B **90**, 73 (1993).
[37] N. Furukwa and M. Imada, J. Phys. Soc. Jpn. **62**, 2557 (1993).
[38] W. Kohn and J. M. Luttinger, Phys. Rev. Lett. **15**, 524 (1965).
[39] G. J. Chen, R. Joynt, F. C. Zhang, and C. Gros, Phys. Rev. B **42**, 2662 (1990).
[40] T. Giamarchi and C. Lhuillier, Phys. Rev. B **43**, 12943 (1991).
[41] F. C. Zhang and T. M. Rice, Phys. Rev. B **37**, 3759 (1988).
[42] L. F. Feiner, J. H. Jefferson, and R. Raimondi, Phys. Rev. B **53**, 8751 (1996).
[43] E. Müller-Hartmann and A. Reischl, Euro. Phys. J. B **28**, 173 (2002).
[44] M. Imada and T. Miyake, J. Phys. Soc. Jpn. **79**, 112001 (2010).
[45] M. Wimmer, ACM Trans. Math. Softw. **38**, 30 (2012).
[46] S. Watanabe and M. Imada, J. Phys. Soc. Jpn. **73**, 1251 (2004).
[47] H. Yokoyama, Y. Tanaka, M. Ogata, and H. Tsuchiura, J. Phys. Soc. Jpn. **73**, 1119 (2004).
[48] C.-C. Chang and S. Zhang, Phys. Rev. Lett. **104**, 116402 (2010).
[49] F. Becca, M. Capone, and S. Sorella, Phys. Rev. B **62**, 12700 (2000).
[50] T. Kashima and M. Imada, J. Phys. Soc. Jpn. **70**, 2287 (2001).
[51] H. Morita, S. Watanabe, and M. Imada, J. Phys. Soc. Jpn. **71**, 2109 (2002).
[52] T. Mizusaki and M. Imada, Phys. Rev. B **74**, 014421 (2006).
[53] P. Corboz, M. Troyer, A. Kleine, I. P. McCulloch, U. Schollwöck, and F. F. Assaad, Phys. Rev. B **77**, 085108 (2008).
[54] T. Misawa and M. Imada, Phys. Rev. B **75**, 115121 (2007).
[55] A. Moreo, D. Scalapino, and E. Dagotto, Phys. Rev. B **43**, 11442 (1991).
[56] E. Plekhanov, S. Sorella, and M. Fabrizio, Phys. Rev. Lett. **90**, 187004 (2003).

[57] D. Sénéchal, A. G. R. Day, V. Bouliane, and A.-M. S. Tremblay, Phys. Rev. B **87**, 075123 (2013).
[58] F. Becca, L. Capriotti, A. Parola, and S. Sorella, in *Introduction to Frustrated Magnetism*, edited by C. Lacroix, P. Mendels, and F. Mila (Springer-Verlag, Berlin, Heidelberg, 2011), Chap. 15.
[59] T. Misawa, K. Nakamura, and M. Imada, Phys. Rev. Lett. **108**, 177007 (2012).
[60] R. Kaneko, S. Morita, and M. Imada, J. Phys.: Conf. Ser. **454**, 012046 (2013).
[61] E. Pavarini, I. Dasgupta, T. Saha-Dasgupta, O. Jepsen, and O. K. Andersen, Phys. Rev. Lett. **87**, 047003 (2001).
[62] W.-J. Hu, F. Becca, and S. Sorella, Phys. Rev. B **85**, 081110 (2012).
[63] A. W. Sandvik, Phys. Rev. B **56**, 11678 (1997).